














Using nebular near-IR spectroscopy to measure asymmetric chemical distributions in 2003fg-like thermonuclear supernovae

J. O’HORA ¹, C. ASHALL ^{1,2}, M. SHAHBANDEH ³, E. HSIAO ⁴, P. HOEFELICH ⁴, M. D. STRITZINGER ⁵,
L. GALBANY ^{6,7}, E. BARON ^{8,9}, J. DERKACY ^{3,1}, S. KUMAR ¹⁰, J. LU ¹¹, K. MEDLER ^{1,2} AND B. SHAPPEE ²

¹*Department of Physics, Virginia Tech, 850 West Campus Drive, Blacksburg, VA 24061, USA*

²*Institute for Astronomy, University of Hawai’i at Manoa, 2680 Woodlawn Dr., Hawai’i, HI 96822, USA*

³*Space Telescope Science Institute, 3700 San Martin Drive, Baltimore, MD 21218-2410, USA*

⁴*Department of Physics, Florida State University, 77 Chieftan Way, Tallahassee, FL 32306, USA*

⁵*Department of Physics and Astronomy, Aarhus University, Ny Munkegade 120, DK-8000 Aarhus C, Denmark*

⁶*Institute of Space Sciences (ICE, CSIC), Campus UAB, Carrer de Can Magrans, s/n, E-08193 Barcelona, Spain*

⁷*Institut d’Estudis Espacials de Catalunya (IEEC), E-08034 Barcelona, Spain*

⁸*Planetary Science Institute, 1700 East Fort Lowell Road, Suite 106, Tucson, AZ 85719-2395 USA*

⁹*Hamburger Sternwarte, Gojenbergsweg 112, D-21029 Hamburg, Germany*

¹⁰*Department of Astronomy, University of Virginia, 530 McCormick Rd, Charlottesville, VA 22904, USA*

¹¹*Department of Physics and Astronomy, Michigan State University, East Lansing, MI 48824, USA*

ABSTRACT

We present an analysis of three near-infrared (NIR; 1.0–2.4 μm) spectra of the SN 2003fg-like/“super-Chandrasekhar” type Ia supernovae (SNe Ia) SN 2009dc, SN 2020hvf, and SN 2022pul at respective phases of +372, +296, and +294 d relative to the epoch of *B*-band maximum. We find that all objects in our sample have asymmetric, or “tilted,” [Fe II] 1.257 and 1.644 μm profiles. We quantify the asymmetry of these features using five methods: velocity at peak flux, profile tilts, residual testing, velocity fitting, and comparison to deflagration-detonation transition models. Our results demonstrate that, while the profiles of the [Fe II] 1.257 and 1.644 μm features are widely varied between 2003fg-likes, these features are correlated in shape within the same SN. This implies that line blending is most likely not the dominant cause of the asymmetries inferred from these profiles. Instead, it is more plausible that 2003fg-like SNe have aspherical chemical distributions in their inner regions. These distributions may come from aspherical progenitor systems, such as double white dwarf mergers, or off-center delayed-detonation explosions of near-Chandrasekhar mass carbon-oxygen white dwarfs. Additional late-phase NIR observation of 2003fg-like SNe and detailed 3-D NLTE modeling of these two explosion scenarios are encouraged.

Keywords: supernovae, type Ia supernovae, white dwarf stars, Chandrasekhar limit, observational astronomy, near-infrared astronomy

1. INTRODUCTION

Type Ia supernovae (SNe Ia) are thermonuclear explosions of carbon/oxygen (C/O) white dwarf (WD) stars in binary systems (Hoyle & Fowler 1960; Hillebrandt & Niemeyer 2000). Despite decades of detailed study, the exact nature of their progenitors and explosion mechanisms are a matter of open debate (Iben Jr & Tutukov

1984; Webbink 1984; Fink et al. 2007; Mazzali et al. 2007; Wang & Han 2012; Holcomb et al. 2013; Liu et al. 2017, 2023). It has long been apparent that SNe Ia are a diverse group comprised of a variety of “peculiar” sub-classes (e.g. Filippenko et al. 1992a,b; Mazzali et al. 1995; Howell 2001; Li et al. 2001, 2003; Ganeshalingam et al. 2012). Some of the SNe Ia within these sub-classes do not follow the luminosity-width relation, suggesting that there are multiple pathways to produce these cosmic explosions (e.g. Livio & Mazzali 2018; Ashall et al. 2021; Liu et al. 2023; Siebert et al. 2023).

One rare sub-class are 2003fg-like/“super-Chandrasekhar” SNe (hereafter “03fg-likes”; [Howell et al. 2006](#)). These objects generally exhibit: *i*) high peak absolute B -band magnitudes spanning the range between $-21 < M_B < -19$ mag; *ii*) broad light curves with decline rates of $\Delta m_{15,B} < 1.3$ mag; *iii*) strong C absorption at maximum light; *iv*) low ejecta velocities; *v*) an i -band light curve peak that occurs after the B -band peak; *vi*) higher luminosities in the near-infrared (NIR) compared to normal SNe Ia; *vii*) a tendency to occur in low-metallicity, low-surface-brightness galaxies; and *viii*) distinct UV colors ([Howell et al. 2006](#); [Childress et al. 2011](#); [Khan et al. 2011](#); [Taubenberger et al. 2019](#); [Ashall et al. 2021](#); [Liu et al. 2023](#); [Hoogendam et al. 2024](#); [Galbany et al. in prep](#)). Some 03fg-like SNe Ia also exhibit an early flux excess (or a “bump”) in their light curves relative to a smooth power-law rise (e.g. [Jiang et al. 2021](#); [Dimitriadis et al. 2023](#); [Siebert et al. 2023](#); [Srivastav et al. 2023](#)).

The precise workings of the progenitor systems and explosion mechanisms of 03fg-like SNe are debated. However, it is generally accepted that these explosions occur within a carbon-rich envelope ([Hachinger et al. 2012](#); [Noebauer et al. 2016](#); [Ashall et al. 2021](#); [Maeda et al. 2023](#)). There are two popular models for explaining this carbon-rich ejecta: *texti*) the violent merger of two C/O WDs ([Webbink 1984](#); [Fink et al. 2007](#); [Pakmor et al. 2010, 2011, 2012](#); [Siebert et al. 2023](#); [Siebert et al. 2023](#); [Srivastav et al. 2023](#); [Kwok et al. 2024](#)), which is naturally asymmetric; or *ii*) the core-degenerate scenario, where a WD merges with the degenerate core of an asymptotic giant branch star ([Livio & Riess 2003](#); [Kashi & Soker 2011](#); [Hsiao et al. 2020](#); [Lu et al. 2021](#)). In the case of the latter, a thermonuclear runaway may occur upon the initiation of a subsonic deflagration flame front, which may then transition to a supersonic detonation flame ([Hoeftich et al. 2019](#); [Soker 2019](#)). In this scenario, the deflagration-to-detonation transition (DDT) occurs on an approximately-spherical expanding background, which results in lower density burning thus asymmetric abundance distributions of burning products produced during the detonation (e.g. [Hoeftich et al. 2021](#); [DerKacy et al. 2023](#); [Ashall et al. 2024](#)).

Overall, both explosion scenarios are capable of producing the high luminosity and C I and C II absorption observed in 03fg-like SNe (e.g. [Lu et al. 2021](#); [Siebert et al. 2023](#); [Kwok et al. 2024](#)); however, each scenario has caveats. In the core-degenerate scenario, it is not clear how the progenitor system would shed its H and He-rich envelope. It is plausible that this could occur through a super-wind phase ([Hsiao et al. 2020](#)). In the violent merger scenario, on the other hand, it is not clear

how this scenario could incorporate a massive C-rich envelope, and further work is also needed to determine if these systems can produce dust (e.g. [Siebert et al. 2023](#); [Kwok et al. 2024](#); [Liu et al. 2025](#)).

Distinguishing between these two progenitor models is not trivial. This is because both scenarios may have an asymmetric chemical distribution in the core of the explosion, which is highly dependent on the triggering mechanism of the explosion and how the flame propagates through the ejecta. Recently, [Liu et al. \(2025\)](#) used optical spectra to infer further information about the explosion mechanism of these events, suggesting that centrally-peaked [C I] 9.824 and 9.850 μm emissions in the 03fg-like SN 2022pul at a phase of +515 d from B -band maximum may indicate a pure deflagration of a super-Chandrasekhar-mass WD ([Liu et al. 2025](#)).

In this work, our attention is focused on late-phase observations in the NIR. Nebular-phase (>250 d) spectra of SNe Ia reveal the inner region of the ejecta, making them a useful resource for analyzing core asymmetry, burning conditions, and explosion physics ([Marietta et al. 2000](#); [Mazzali et al. 2007](#); [Maeda et al. 2010](#); [Hoeftich et al. 2021](#); [Kumar et al. 2023](#); [Dimitriadis et al. 2023](#); [Kumar et al. 2023](#); [Ashall et al. 2024](#); [Bose et al. 2025](#); [Liu et al. 2025](#)). Furthermore, the NIR is a useful yet underutilized wavelength region compared to the optical, since it provides a different set of spectral features and exhibits less line blending. For example, the [Fe II] emission lines at 1.257 and 1.644 μm have been shown to provide measurements of explosion kinematics, WD central density, and magnetic fields in normal SNe Ia ([Penney & Hoeftich 2014](#); [Diamond et al. 2015, 2018](#); [Maguire et al. 2018](#); [Hoeftich et al. 2021](#); [Kumar et al. 2023](#)). To date, SN 2009dc and SN 2022pul are the only 03fg-like SNe with a published nebular-phase-NIR spectrum ([Taubenberger et al. 2013](#); [Siebert et al. 2023](#); [Kwok et al. 2024](#)). Moreover, no work thus far has analyzed a sample of 03fg-likes in both the NIR and at nebular phases to look for similarities between the explosions.

Here, we analyze NIR nebular spectra of SN 2009dc and SN 2022pul in conjunction with a new NIR nebular spectrum of the 03fg-like SN 2020hvf. In Section 2, we present details of the observations, as well as data reduction when appropriate. In Section 3, we discuss the lines that contribute to the spectra, as well as the shapes of the spectral features. In Section 4, we compare the spectroscopy of 03fg-like SNe to each other and normal SNe Ia, with specific emphasis on the asymmetric line profiles of the 03fg-likes. Section 4 also presents five analytical methods to quantitatively describe these profile asymmetries: Section 4.2 presents our measurements

of the velocities at peak flux for the 03fg-like and normal SNe; Section 4.3 quantifies the degree of asymmetry/tilting in the 03fg-like features; Section 4.4 presents a residual test between the [Fe II] 1.644 μm lines of each 03fg-like with each normal SN Ia; Section 4.5 discusses a curve-fitting procedure for the 03fg-like spectra that visualizes the individual components of the complexes around 1.26 and 1.64 μm with Gaussian functions; and lastly, in Section 4.6 we compare the 1.644 μm features of the 03fg-likes to pre-existing spectral models of off-center delayed-detonation explosions. Our conclusions are presented in Section 5.

2. OBSERVATIONS & DATA REDUCTION

For this work we searched the literature for NIR spectra of 03fg-like SNe in the nebular phase ($>+250$ d). To our knowledge, only SN 2009dc and SN 2022pul have such published observations. We analyze these spectra along with a new NIR nebular phase spectrum of SN 2020hvf, giving us a total of three nebular-NIR spectra of 03fg-like SNe. To emphasize the differences in spectral profiles between 03fg-like and normal SNe Ia, we also analyze NIR nebular phase spectra of SNe Ia 2013aa and 2017cbv (Kumar et al. 2023). We choose these objects because they are well observed and their nebular phase spectra are representative of normal SNe Ia, which generally exhibit highly symmetric [Fe II] line profiles (Diamond et al. 2015, 2018; Kumar et al. 2023; Kumar 2024, Kumar et al., in preparation). Table 1 presents the full log of observations used throughout this work.

The NIR spectrum of SN 2020hvf was obtained using the Near-Infrared Echellette Spectrometer (NIREs) instrument on the Keck II telescope on 2021 March 4.40 UT (MJD 59277.4). This date corresponds to a rest-frame phase of +296.4 d from the epoch of *B*-band maximum which occurred on MJD 58979.3 (Jiang et al. 2021). The spectrum covers the wavelength region between $0.97\mu\text{m} \sim 2.47\mu\text{m}$. The total exposure time of the observations was 7200 s from 6 sets of ABBA observations, where each individual A/B exposure lasted 300 s. The data was reduced with the IDL package Spextools version 5.0.2 (Cushing et al. 2004). Flux calibration and telluric feature corrections were completed with Xtellcorr version 5.0.2 via observations of the A0V star HIP56736. Throughout this work, spectral resolution has been accounted for when reporting velocity measurements.

3. LINE IDENTIFICATIONS

Figure 1 presents the NIR spectra of SNe 2009dc, 2020hvf, and 2022pul at respective phases of +372 d, +296 d, and +294 d from *B*-band maximum, which we adopt in this work as the standard reference for phase. Using the line lists from Hoefflich et al. (2021), Blondin et al. (2023), and Kwok et al. (2024), we identify the strongest lines that may contribute to each spectral feature. Our line IDs are listed in Table 2. We discuss these lines from the bluer to the redder wavelengths below. Future modeling is required to ascertain exactly which lines contribute to the spectral formation and what strengths these lines have.

The strong peak at the bluest ends of all spectra can be attributed to a blend of [Co II] 1.019 and [S II] 1.032 μm . This complex is difficult to identify in SN 2009dc due to noise. For all SNe, a blended complex spans the wavelength region between 1.24-1.34 μm . The bluer end of this complex is dominated by emission associated with [Fe II] 1.257 μm . Weak [Ni II] 1.278 μm is observed in all three SNe just redwards of the 1.257 μm line; we also observe weak [Co III] 1.310 μm in SN 2020hvf and SN 2022pul only. Moving redward, there exists weak [Fe II] 1.534 μm and [Si I] 1.588 μm emissions. Strong [Fe II] 1.644 μm emission is observed in all SNe. Finally, very weak [Fe III] 2.022 and 2.219 μm emissions are observed at the reddest ends of all three spectra. Overall, the weakness of higher-ionization lines (namely [Fe III]) in tandem with the strengths of singly-ionized features from the same elements suggest a low ionization state for the 03fg-like SNe relative to normal SNe Ia. This aligns closely with optical observations of other 03fg-like SNe at these phases (Silverman et al. 2011; Taubenberger et al. 2013, 2019; Ashall et al. 2021).

While it may be possible that the line profiles at 1.257 and 1.644 μm have some contribution from [Fe II] 1.271 μm , [Si I] 1.646 μm , [Fe II] 1.664 μm , and/or [Fe II] 1.667 μm we determine this is unlikely. This is because these emissions are expected to be very weak in comparison to [Fe II] 1.257 and 1.644 μm (Diamond et al. 2015; Hoefflich et al. 2021) and, if these lines were in fact dominant, there would not be similarity in profile shape in the 1.257 and 1.644 μm regions (see Section 4).

4. SPECTRAL ANALYSIS

4.1. Spectral Profiles

As mentioned before, the [Fe II] 1.257 and 1.644 μm lines have been shown to be useful in quantitative analyses of SNe Ia (Penney & Hoefflich 2014; Diamond et al. 2015, 2018; Maguire et al. 2018; Hoefflich et al. 2021; Ku-

Table 1. Log of observations used in this work.

SN	RA (J2000)	Dec (J2000)	Subtype	z	Phase ^a	Telescope+Instrument	Resolution	Reference
2009dc	15:51:12.12	+25:42:28.00	03fg-like	0.0214	+372	VLT+XShooter	5573	<i>b</i>
2013aa	14:32:33.88	−44:13:27.80	Normal	0.0040 ^c	+365	Magellan Baade+FIRE	1200	<i>d</i>
2017cbv	14:32:34.42	−44:08:02.74	Normal	0.0040 ^c	+307	Magellan Baade+FIRE	1200	<i>d</i>
2020hvf	11:21:26.45	+03:00:52.85	03fg-like	0.0058	+296	Keck II+NIRES	2700	This work
2022pul	12:26:49.00	+08:26:55.25	03fg-like	0.0030	+294	Keck II+NIRES	2700	<i>e</i>

NOTE—^a Rest-frame days relative to the epoch of B -band maximum; ^b Taubenberger et al. (2013); ^c Additional corrections are made for the motion of the SN within the galaxy (see Kumar et al. 2023 for more details); ^d Kumar et al. (2023); ^e Siebert et al. (2023).

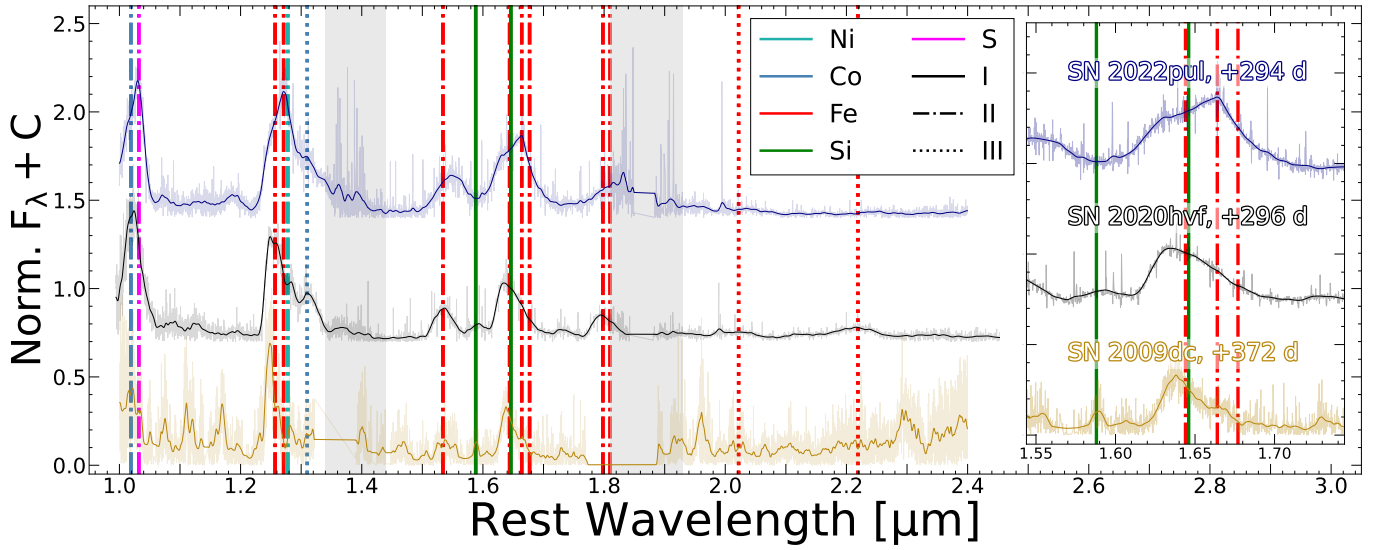


Figure 1. Full NIR spectra of SN 2009dc, SN 2020hvf, and SN 2022pul at nebular phases. Spectra are redshift-corrected (Table 1), offset from each other, and overlaid with a smooth 1D Gaussian-filtered solid curve with a smoothing length of 12 pixels. Prominent spectral features are marked, with color- and style-coding by ionic species. Telluric regions are highlighted in light gray. The inset identifies many lines that could contribute to the feature around $1.6 \mu\text{m}$ for each 03fg-like SN presented. However, as discussed in the text (Section 4.3), we identify [Fe II] $1.644 \mu\text{m}$ as the dominant ion in this region.

mar et al. 2023). For normal SNe Ia, these lines typically exhibit a high degree of symmetry.

In the 03fg-like SNe, however, both features around the [Fe II] 1.26 and $1.64 \mu\text{m}$ regions show a clear asymmetry, appearing as a “tilt” in their peaks. Furthermore, for each SN, the directions and morphologies of these tilts appear to be consistent between the 1.257 and $1.644 \mu\text{m}$ features (see Fig. 2). For this similarity in tilting between features to be caused by line blending would be an unlikely case; this suggests that [Fe II] is the dominant ion contributing to the spectral formation in both features, in particular [Fe II] 1.257 and $1.644 \mu\text{m}$ emissions.

To better qualitatively compare the differences in the [Fe II] 1.257 and $1.644 \mu\text{m}$ features amongst our

SNe, Fig. 2 presents these features in velocity space for each 03fg-like SN in our sample along with SNe 2013aa (+365 d) and 2017cbv (+307 d). The phases of these spectra are each representative of similar late-phase ionization states for SNe Ia, hence providing solid ground for spectral comparison. For the normal SNe, the peaks of the [Fe II] 1.257 and $1.644 \mu\text{m}$ lines are very close to zero velocity; however, in the 03fg-like SNe, the peaks of these features are largely offset from zero velocity by up to $\sim \pm 3000 \text{ km s}^{-1}$. Additionally, the shapes of the line profiles vary between SNe; SN 2009dc and 2020hvf exhibit blue-peaked tilts, while SN 2022pul exhibits red-peaked tilts.

4.2. Profile Peaks

Table 2. List of identified spectral lines

λ (μm)	Ion	λ (μm)	Ion	λ (μm)	Ion	λ (μm)	Ion	λ (μm)	Ion
0.994	[Co II]	1.046	[Ni II]	1.298	[S III]	1.547	[Co II]	1.725	[Ni II]
1.019	[Co II]	1.131	[Si I]	1.310	[Co III]	1.588	[Si I]	1.741	[Fe II]
1.021	[Ni II]	1.191	[Fe II]	1.321	[Fe II]	1.644	[Fe II]	1.745	[Fe II]
1.024	[Co II]	1.257	[Fe II]	1.328	[Fe II]	1.646	[Si I]	1.798	[Fe II]
1.028	[Co II]	1.271	[Fe II]	1.372	[Fe II]	1.664	[Fe II]	1.810	[Fe II]
1.029	[S II]	1.278	[Ni II]	1.525	[Fe II]	1.677	[Fe II]	2.022	[Fe III]
1.032	[S II]	1.294	[Fe II]	1.534	[Fe II]	1.712	[Fe II]	2.219	[Fe III]

NOTE—Line identifications are chosen based on radiation transport models from [Hoeftich et al. \(2021\)](#) and [Blondin et al. \(2023\)](#).

To better understand the shape of the spectral profiles, we first measure the velocity at peak flux of the features without making any assumptions about the shape of the emitting region or the number of different components and ions which contribute to it. This is because the emitting region could be spherical, asymmetric, or ring-like and still be produced from emission dominated by a single ion (e.g. [Mazzali et al. 2007](#); [Jerkstrand 2017](#); [Hoeftich et al. 2021](#); [Ashall et al. 2024](#)). For example, the merger of two WDs may produce a ring-like structure and double-horned profiles ([Jerkstrand 2017](#); [Hoeftich et al. 2021](#)). Moreover, the suppression of the red component of a spectral feature could also result from the obstruction of flux originating from an extended photosphere ([Penney & Hoeftich 2014](#)).

To obtain measurements of the velocity at peak flux, we smooth the data using a 1-D Gaussian filter with a smoothing length of 10 pixels. The residual between an individual raw data point F_i and this Gaussian-smoothed data is treated as one standard deviation of error σ_i . For 500 iterations, a new “perturbed” smooth curve is then constructed from the original smooth curve by varying each F_i by an amount randomly sampled from a normal distribution with standard deviation σ_i . The velocity at the absolute maximum of this perturbed smooth curve is then measured for each iteration, giving us a sample of 500 peak velocity values. The mean and standard deviation of this sample thus constitutes our measurement of the velocity at the peak flux of the line.

Figure 3 presents the results of this fitting procedure for all three of our 03fg-like SNe, plus SNe 2013aa and 2017cbv. From this plot, velocity at peak flux seems to vary over a range of -2000 km s^{-1} to 3000 km s^{-1} within the sample of SNe. Furthermore, there is strong agreement between velocities at peak flux for the 1.257 and $1.644 \mu\text{m}$ features for each 03fg-like SN. The fact that these peaks are simultaneously blue-/red-shifted the same way for each 03fg-like SN we analyze suggests

Table 3. Measurements of velocity at peak flux for asymmetric features.

SN	$1.257 \mu\text{m}$	$1.644 \mu\text{m}$
SN 2009dc	−1940 (240)	−1080 (150)
SN 2013aa	120 (300)	−400 (310)
SN 2017cbv	310 (340)	240 (340)
SN 2020hvf	−1890 (140)	−1562 (320)
SN 2022pul	3455 (290)	3448 (280)

NOTE—Velocities at peak flux for the 1.257 and $1.644 \mu\text{m}$ features, given in km s^{-1} , with uncertainties in parentheses. The methods used in obtaining these values are detailed in Section 4.2.

that chemical asymmetries within the Fe-rich core of the ejecta may be a common characteristic of 03fg-like SNe. Conversely, our values for velocity at peak flux in the normal SNe Ia are not asymmetric, as they are close to $\sim 0 \text{ km s}^{-1}$, demonstrating that the profile asymmetries seen in 03fg-like SNe are distinct.

4.3. Profile Tilts

The 03fg-like SNe in the sample also have varying degrees of asymmetry, or tilt, across the spectral regions of interest. Quantifying this tilt may provide important information about the chemical distributions of 03fg-like SNe, as well as provide a useful parameter for future observations. We hereafter refer to tilt symbolically as m_T . To quantify m_T , we use a Monte Carlo (MC) fitting method, where we calculate the slope of a straight line fitted to the skewed top portion of the feature. The sign and magnitude of the slope respectively describe the direction and steepness of m_T , where we define positive m_T to be a red-peaked slope.

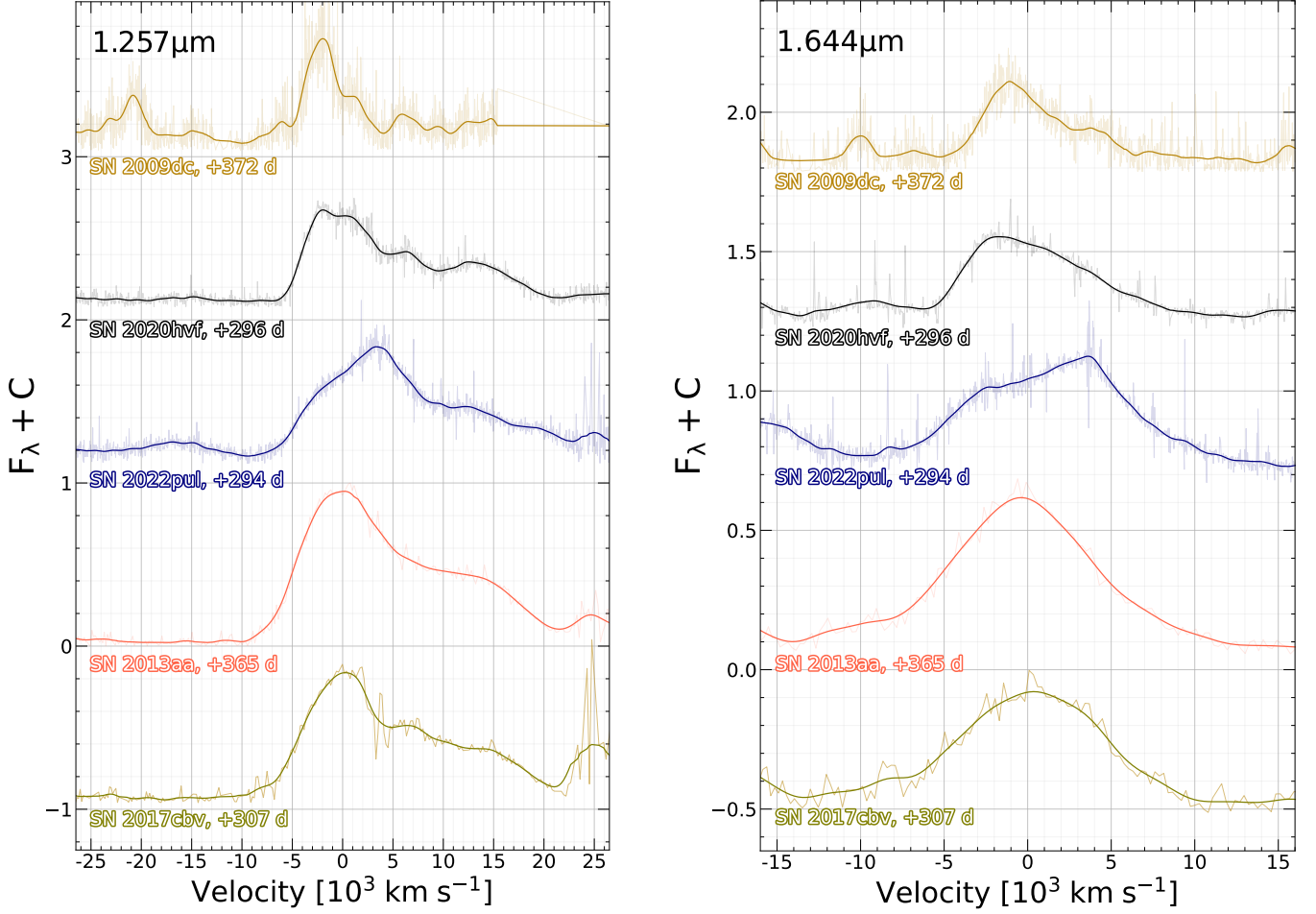


Figure 2. The spectra presented in Table 1 zoomed in on the [Fe II] 1.257 (left) and 1.644 μm (right) features and plotted in velocity space. Again, spectra are redshift-corrected, offset, and overlaid with a 1D Gaussian-filtered smooth curve.

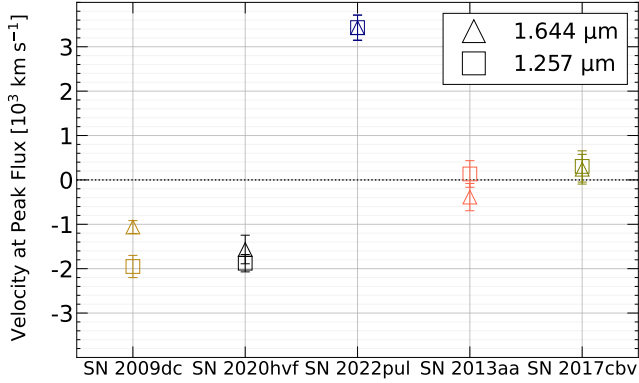


Figure 3. Velocity at peak flux of the [Fe II] 1.257 and 1.644 μm features of each SN, which are measured via the procedure described in Section 4.2. 03fg-like SNe have peaks that are non-zero but consistent between SNe, whereas the normal SNe velocities at peak flux are roughly consistent with 0 km s^{-1} . The peak values plotted here are tabulated in Table 4.

Each MC iteration is constructed using the same method described in Section 4.2. However, for each iteration, we fit the tilted top of the perturbed smooth profile with a straight line, where the bounds on this linear fit are manually defined to be the locations of the two outer edges of the tilted top of the feature. We call the velocity separation between these two bounds Δv , and we determine its uncertainty the same way as the velocity at peak flux. We conduct 500 iterations of this process, where the mean and standard deviation of the sample of slopes taken from each linear fit are our measurement of m_T in the 1.257 or 1.644 μm line.

In addition, we choose to examine the percent-change in flux relative to feature maximum $\% \Delta F_\lambda$ across Δv in order to quantitatively compare the 1.257 and 1.644 μm regions. Our measurements of m_T , Δv , and $\% \Delta F_\lambda$ are listed in Table 4 and shown graphically in Fig. 4.

The top panel of Fig. 5 plots the values of m_T for each feature in each 03fg-like SN. We observe an agreement in tilt between the 1.257 and 1.644 μm features

in SN 2020hvf and SN 2022pul, but a large disparity in m_T exists between these features in SN 2009dc. This disparity may be attributed to spectral line blending in SN 2009dc at about 4000 km s⁻¹ redwards of 1.644 μ m that artificially “raises” the red edge of the MC line fits, resulting in a positive skew for m_T . Conversely, the peak of the 1.257 μ m feature in SN 2009dc may be unusually strong, resulting in m_T being more negative.

The bottom panel of Fig. 5 plots the absolute percentage change in flux against the velocity separation between the outer edges of the tilted top for each SN. The absolute percentage change in flux is similar between the 1.257 and 1.644 μ m features for each 03fg-like SN, with the exception of SN 2022pul. Generally, no correlation between $|\% \Delta F_\lambda|$ and Δv is observed between SNe. This implies that, for tilted features with similar widths, a range of changes in flux across the tilt are possible. However, the overall consistency in tilting across features for each SN suggests that these profiles are not dominated by spherical [Fe II] emission, but rather asymmetric [Fe II] emission from an aspherical chemical distribution in the core of the ejecta. Future detailed NLTE spectral modeling is encouraged to corroborate this further.

4.4. Residual-Testing 03fg-like Features Against Normal SNe Ia

To further differentiate the line profiles of 03fg-like SNe from those of normal SNe, we examine the residuals between the 1.644 μ m features of 03fg-like SNe and standard SNe Ia. This allows us to graphically demonstrate how the 1.644 μ m features of 03fg-like SNe deviate from a symmetric profile, and thus how their ejecta deviate from a spherical chemical distribution. Residual testing can also provide useful hints on what features may exist in 03fg-like SNe that distinguish them from normal SNe Ia; however, we limit this analysis to the 1.644 μ m feature since it is symmetric and exhibits minimal blending in the normal SNe.

1-D Gaussian filtering is again used to smooth each 03fg-like and normal SN spectrum. In preparing each residual test, the smoothed normal SNe spectra are each scaled by eye such that the tails of the CN 1.644 μ m lines match up with those of the 03fg-like they are being compared to; this is done without shifting the spectrum itself horizontally. All smoothed spectra are then normalized to 1 at peak flux, leaving two normal 1.644 μ m features and one 03fg-like 1.644 μ m feature superimposed with each other.

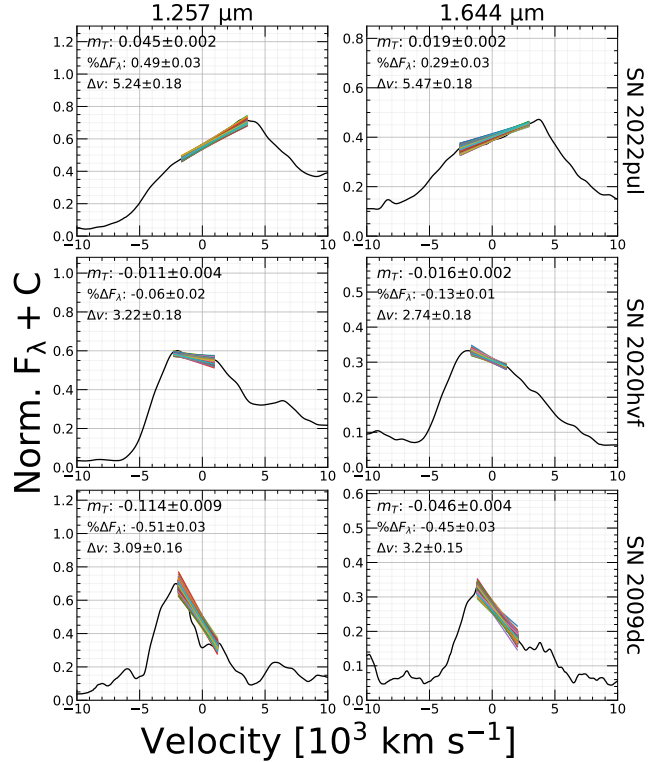


Figure 4. Visualization of the results of the MC tilt measurements described in Section 4.3. Individual spectra are replaced with a 1D Gaussian-filtered smooth curve with smoothing length of 9 pixels to improve the visibility of each MC line fit across the tilt of each feature.

As such, for residual testing to be possible computationally, the normal SN spectra are interpolated to have the same resolution as the 03fg-like spectra. This way, direct calculations of residuals are possible.

Figure 6 shows the results of the residual tests of each 03fg-like SN against SNe 2013aa and 2017cbv. For each 03fg-like SN, its residual against SN 2013aa is similar to the residual against SN 2017cbv. The residual pattern varies widely with each 03fg-like SN, however. SN 2009dc has a significant negative residual just redwards of 1.644 μ m produced by the large tilt on the feature, with a minimum at 2000 km s⁻¹. SN 2020hvf aligns somewhat closely with the normal SNe on its red side, but exhibits a steeper tilt on its blue side, leading to a minimum flux at -5500 km s⁻¹. SN 2022pul has a very large negative residual centered at 0 km s⁻¹, and an even larger positive residual across its entire red side peaking between 4000-6000 km s⁻¹.

Overall, there is no pattern to the residual shapes of SN 2009dc, SN 2020hvf, and SN 2022pul. This suggests that there may be a continuum of viewing angle effects and/or shapes of asymmetric chemical distributions in the cores of 03fg-like SNe ejecta. Further residual test-

Table 4. Measurements of asymmetric feature morphology.

SN	1.257 μm			1.644 μm		
	m_T	$\%\Delta F_\lambda$	$\frac{\Delta v}{10^3 \text{ km s}^{-1}}$	m_T	$\%\Delta F_\lambda$	$\frac{\Delta v}{10^3 \text{ km s}^{-1}}$
SN 2009dc	-0.114 (0.009)	-0.51 (0.03)	3.09 (0.16)	-0.046 (0.004)	-0.45 (0.03)	3.20 (0.15)
SN 2020hvf	-0.011 (0.004)	-0.06 (0.02)	3.22 (0.18)	-0.016 (0.002)	-0.13 (0.01)	2.74 (0.18)
SN 2022pul	0.045 (0.002)	0.49 (0.03)	5.24 (0.18)	0.019 (0.002)	0.29 (0.03)	5.47 (0.18)

NOTE—Tilt m_T is the degree to which the asymmetry in the feature tilts; percent change in flux $\%\Delta F_\lambda$ is the ratio of the flux at the red peak and the flux at the blue peak of the asymmetric feature; velocity separation Δv is the difference in velocity space between the red and blue peaks of the feature. Uncertainties for these values are recorded in parentheses; the methods used in obtaining them are detailed in Section 4.3.

ing of a larger sample of 03fg-like SNe is thus encouraged, especially considering its ability to visualize the full profile rather than just its peak or tilt.

4.5. Velocity Fitting

To quantify line asymmetries further, we fit the profiles in the 1.26 and 1.64 μm regions with analytical functions, which has been done for other SNe in the nebular phase (e.g. Maguire et al. 2018; Tucker et al. 2020; DerKacy et al. 2023; Ashall et al. 2024). We note that this is likely an oversimplification of the problem, as it assumes that the features are produced from multiple symmetric line profiles, whereas 03fg-like SNe are likely to be composed of asymmetric chemical distributions that give rise to inherently non-symmetric line profiles (for observational examples of this, see Hoefflich et al. 2021 and Kwok et al. 2024). Nonetheless, we still choose to provide these fits for consistency, as it is especially applicable for analyses of spectral features with minimal blending (Diamond et al. 2018; Maguire et al. 2018; Kumar et al. 2023; Siebert et al. 2023).

We fit the data in the two regions of interest (1.257 and 1.644 μm) under the assumption that the [Fe II] 1.257 and 1.644 μm transitions can both be characterized by two separate emitting regions that are each approximately Gaussian. We make the same assumption for emissions from other byproducts of ^{56}Ni , such as Co, but not necessarily for stable Ni itself. These weaker lines which contribute to the flux in these regions are based on our line identifications from Section 3.

The fits themselves follow a procedure similar to those described in Diamond et al. (2018), Maguire et al. (2018), Siebert et al. (2020), Kumar et al. (2023), and Siebert et al. (2023). The fitting process begins by subtracting a manually-bounded linear continuum from the feature. We then fit Gaussians to the continuum-subtracted feature with the PYTHON tool CURVE_FIT()

from the SCIPY.OPTIMIZE library (Jones et al. 2001; Fadillah et al. 2021). This tool produces optimal parameters and covariances on these parameters for each Gaussian component of the fit. The error on each parameter is then taken to be the square root of its covariance with itself. We allow up to 1000 χ^2 iterations, where each Gaussian can vary in width, strength, and peak position independently of the ion producing the transition. We then convert to velocity space the best-fit parameters for mean (hereafter v_{peak}) and standard deviation (which is also converted to FWHM and henceforth called v_{width}).

The graphical results of our Gaussian fits to the [Fe II] 1.644 μm features are displayed in the right column of Fig. 7. Each fit recreates its corresponding profile. The component with the largest amplitude also aligns with the peaked side of the feature, which is the blue side for SN 2009dc and SN 2020hvf and the red side for SN 2022pul.

The left column of Fig. 7 shows the results of our Gaussian fits to the [Fe II] 1.257 μm features. In contrast to the 1.644 μm feature, there is blending around this complex; furthermore, the features that are blended vary between each 03fg-like SN. This results in different ionic species being identified for different SNe in the 1.257 μm region. For instance, every 03fg-like SN is fitted with a singular [Ni II] 1.278 μm line just redwards of the ubiquitous [Fe II] 1.257 μm lines; however, only SN 2020hvf and SN 2022pul are fitted with two [Co III] 1.310 μm lines. In the case of a singular [Ni II] component, which produces the best fits, this is physically permissible, but we cannot rule out double [Ni II] emissions.

The numerical results for v_{peak} and v_{width} from our Gaussian fits are shown in Fig. 8, which plots v_{peak} against v_{width} for each Gaussian representing [Fe II] 1.257 or 1.644 μm emissions for each 03fg-like SN, along

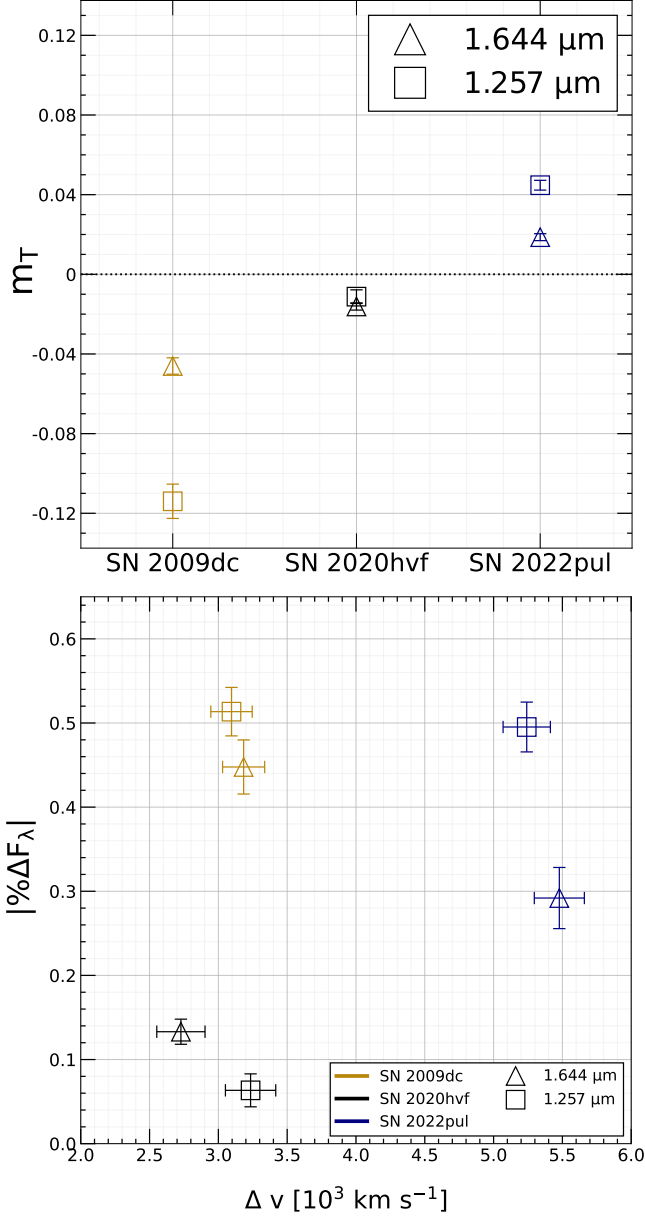


Figure 5. *Top:* Tilt m_T of the [Fe II] 1.257 and 1.644 μm features of each 03fg-like SN, which are measured via the procedure described in Section 4.3. The tilts are consistent across features for SN 2020hvf and mostly consistent for SN 2022pul, but not for SN 2009dc, the reasons for which are discussed in Section 4.3 (See also Table 4 and Fig. 4). *Bottom:* Comparison of absolute $\% \Delta F_\lambda$ and Δv , which are measured by the procedures explained in Section 4.3. No correlation is observable here, suggesting that asymmetric features have varied changes in flux between their edges, regardless of Δv .

with those of each 1.644 μm component for each normal SN. For clarity, we define “coupled” components to be the red and blue members of a double Gaussian fit corresponding to a singular spectral feature that is tilted. While it may seem natural to explain such coupled components as arising from two separate emitting spheres (i.e. a merger of two WDs), we stress here that this may not be the true physical composition of the ejecta. Multiple Gaussian emissions may still be an analytical way of explaining line profiles occurring from asymmetric chemical distributions. Only through detailed modeling, however, can this issue be disentangled. Regardless of their true nature, these coupled components allow us to examine the nonspherical nature of the emitting region. We report that in each of our 03fg-like SNe the difference in v_{peak} between coupled components is consistent in both the 1.257 and 1.644 μm features.

For SN 2020hvf the blue components center around $\sim -2500 \text{ km s}^{-1}$, and the red components $\sim 1000 \text{ km s}^{-1}$, making a separation of $\sim 3500 \text{ km s}^{-1}$. SN 2022pul has a larger separation of $\sim 6000 \text{ km s}^{-1}$, with the blue components centered around $\sim 3000 \text{ km s}^{-1}$ and the red components $\sim 3000 \text{ km s}^{-1}$. The split for SN 2009dc is more uncertain due to the low SNR of the spectrum, which makes it difficult to properly fit the weaker lines in the feature. Nonetheless, the split between the features is approximately $\sim 4000 \text{ km s}^{-1}$.

As Siebert et al. (2023) performed a similar procedure for fitting the optical Fe/Ni/Ca complex at $\sim 7300 \text{ \AA}$ for SN 2020hvf, we discuss how our results compare. One difference between the analysis of Siebert et al. (2023) and our work is that Siebert et al. (2023) add the additional constraint that the values of v_{width} are the same between coupled [Fe II] 0.7155 μm components. This is because the optical lines are much more blended than the NIR lines, so the relative widths cannot feasibly be determined. Siebert et al. (2023) obtained a $\sim 3000 \text{ km s}^{-1}$ velocity separation between coupled [Fe II] 0.7155 μm components at a phase of +277 d, which agrees well with our results for the velocity separation between coupled components of [Fe II] 1.257 and 1.644 μm at +294 d. However, since our methods do not constrain v_{width} to be uniform between coupled components, we obtain $v_{\text{width}} \approx 3500 \text{ km s}^{-1}$ for the blue components and $\sim 4500 \text{ km s}^{-1}$ for the red components. Furthermore, Siebert et al. (2023) reported a $\sim 2700 \text{ km s}^{-1}$ separation between coupled [Ni II] 0.7378 μm emissions; in our data we find no strong need for a double Ni component in SN 2020hvf, but we reiterate that we cannot rule this out either.

4.6. Off-Center Delayed-Detonation Explosion Models

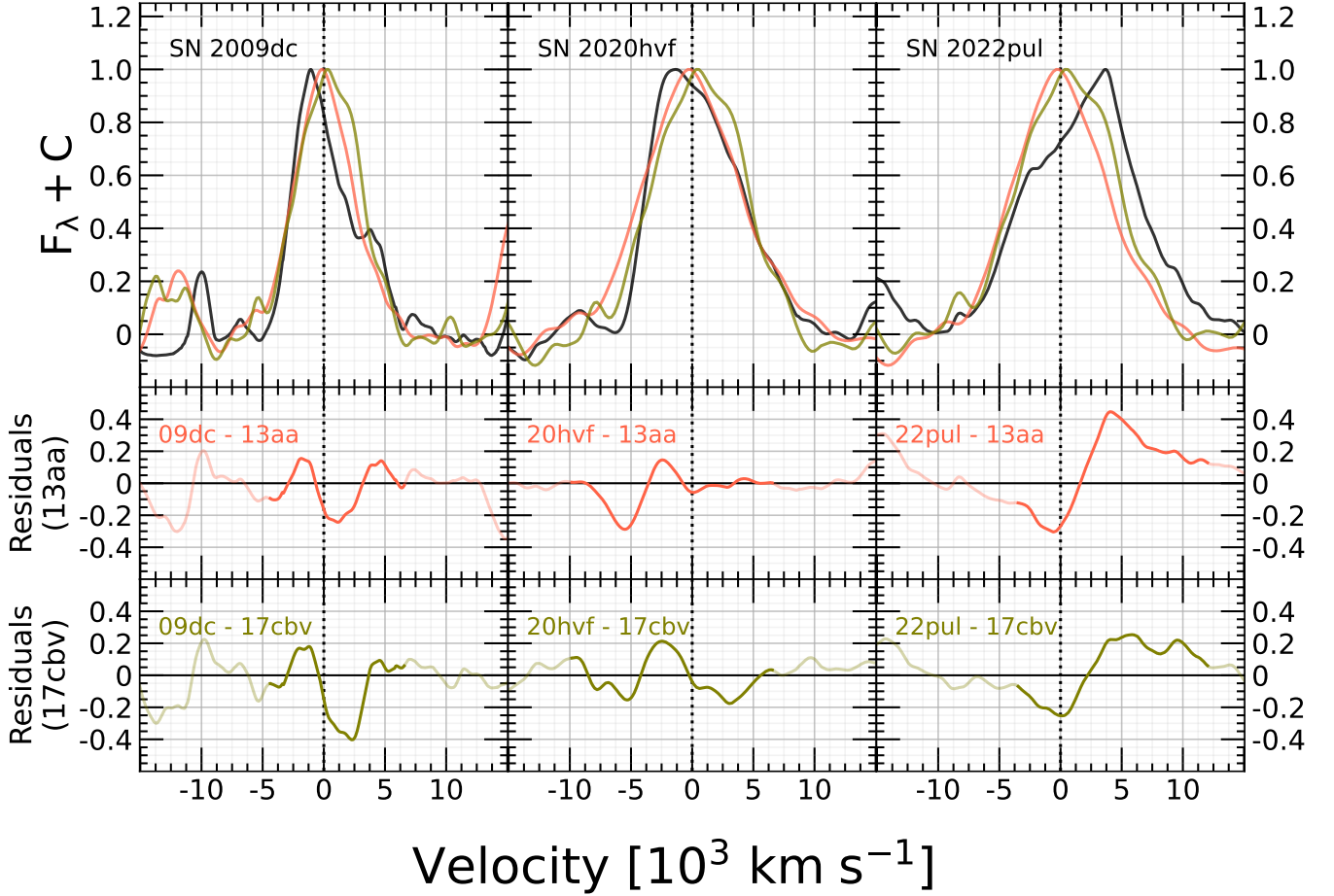


Figure 6. Residual plots of the $1.644 \mu\text{m}$ features of SN 2009dc, SN 2020hvf, and SN 2022pul (black) against those of both SN 2013aa (red) and SN 2017cbv (green). The procedure for obtaining these residual plots is detailed in Section 4.4. Highlighted regions in the bottom two rows represent the most significant deviations in profile shape for each 03fg-like SN.

As discussed previously, one way to produce asymmetric line profiles in a SN Ia explosion is through an off-center delayed detonation explosion (Hoeftlich et al. 2021). In the context of 03fg-like SNe, this may occur in the core degenerate scenario. Previous modeling efforts on 03fg-like SNe have shown that a DDT may be a key component to explaining their peculiarities (e.g. Hsiao et al. 2020; Lu et al. 2021). In off-center DDTs, the ignition starts near the center and the flame propagates as a deflagration before transitioning to a detonation at a specific mass coordinate. This off-center DDT can thus produce asymmetric chemical distributions and, by extension, off-center line profiles for various viewing angles (Hoeftlich et al. 2017; Hoeftlich et al. 2021; DerKacy et al. 2023; Ashall et al. 2024).

As it is outside the scope of this work to produce new models specific for 03fg-like SNe Ia, we visually compare the $1.644 \mu\text{m}$ lines of our 03fg-likes with DDT models created by Hoeftlich et al. (2021) in their analysis of the under-luminous type Ia SN 2020qxp, which

also exhibits an asymmetric $1.644 \mu\text{m}$ line. These models demonstrate tilting in the $1.644 \mu\text{m}$ line due to an asymmetric chemical distribution produced by an off-center DDT observed from various viewing angles (-90° , -30° , 0° , $+30^\circ$, and $+90^\circ$) relative to the equator (see Hoeftlich et al. 2021 for more details). Although they are located in different areas of the luminosity width relation, both SN 2020qxp and 03fg-like SNe Ia have low ionization states relative to normal SNe Ia, and hence similar core structures (Lu et al. 2021; Hoeftlich et al. 2021). Thus, these models make a useful reference for testing this explosion scenario against the diverse range of data for our 03fg-like SNe.

Despite having similar ionization states, SN 2020qxp and 03fg-like SNe have significant differences in luminosity, ^{56}Ni mass, and Fe distributions. Hence, the model [Fe II] $1.644 \mu\text{m}$ lines have to be modified to align with those of the 03fg-like spectra in order to control for these variables. In short, we scale and shift the flux of each model vertically so that the peaks of the model and the

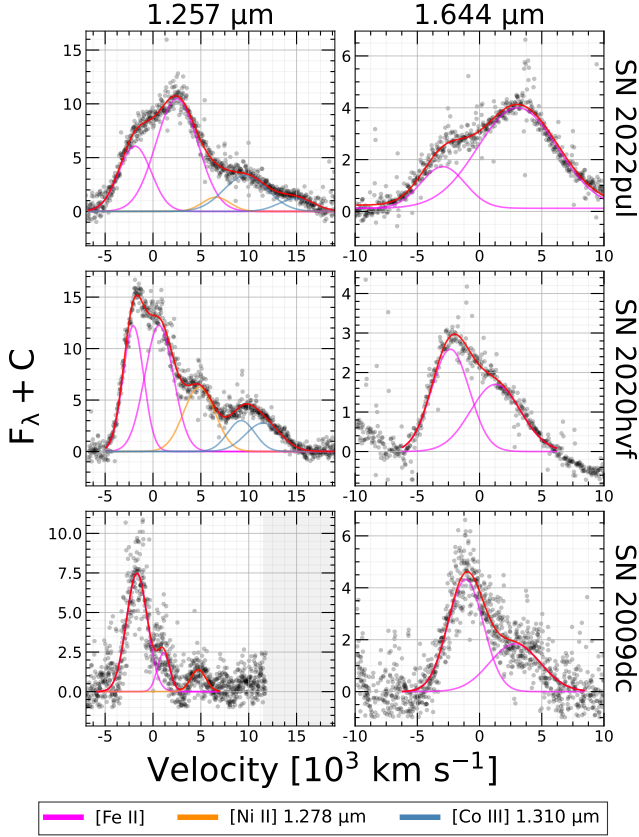


Figure 7. Gaussian curve fitting results for the $1.644 \mu\text{m}$ and $1.257 \mu\text{m}$ features of our 03fg-like SNe. The gray region past $\sim 11000 \text{ km s}^{-1}$ for the $1.257 \mu\text{m}$ feature of SN 2009dc is a telluric region left unobserved by the XShooter instrument (Table 1).

data align in flux, controlling for luminosity; the widths of the models are also augmented to match the 03fg-likes, which controls for ^{56}Ni mass (which is a strong predictor of [Fe II] feature width). We overlay the DDT models with the $1.644 \mu\text{m}$ features of our 03fg-like SNe in Fig. 9. The choice of viewing angle for each DDT model being overlaid is based on its visual agreement with the tilt of the 03fg-like.

There is good agreement between the -90° model and SN 2022pul, as well as good agreement between the $+90^\circ$ model and SN 2020hvf, supporting the idea that these objects may come from such an explosion scenario. On the other hand, for SN 2009dc, no model aside from $+90^\circ$ comes close to matching the profile shape. This may be a consequence of SN 2009dc having a different central density than SN 2020qxp, as the central density of the model determines the width of the tilted peak (Hoeftlich et al. 2021). It is also possible that SN 2009dc is better explained by a completely separate explosion mechanism.

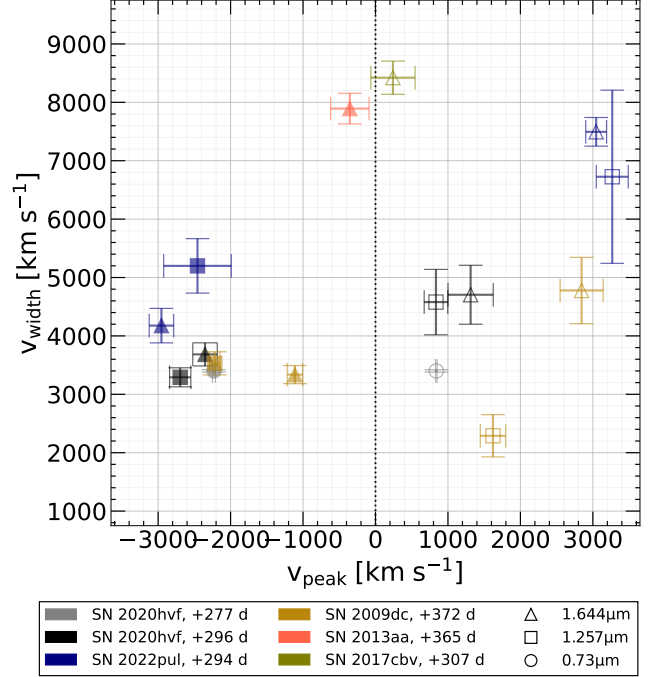


Figure 8. v_{width} plotted against v_{peak} for each Gaussian corresponding to the [Fe II] 1.257 or $1.644 \mu\text{m}$ feature of each SN. Fit results for SNe 2013aa and 2017cbv are obtained from Kumar et al. (2023), while fit results for the [Fe II] $0.73 \mu\text{m}$ feature of SN 2020hvf are from Siebert et al. (2023). All measurements are made using a procedure similar to that described in Section 4.5. The consistent separations in velocity between coupled components of the [Fe II] features of the 03fg-likes are indicative of asymmetric chemical distributions in the cores of these explosions. No significant velocity offset, however, is observed in the [Fe II] $1.644 \mu\text{m}$ features of the normal SNe.

Further modeling of off-center explosion models are encouraged for more robust model comparison tests of other peculiar SNe Ia like SN 2009dc.

5. CONCLUSIONS

We present an analysis of three NIR spectra of 03fg-like SNe in the nebular phase. Before this work, only two such spectra existed in the literature (Taubenberger et al. 2011; Siebert et al. 2023), where we contribute the third. While these nebular NIR spectra are a rare resource, we demonstrate that they are a powerful tool for determining the underlying physics in the explosion. Specifically, we find that all three SNe in our sample show asymmetric line profiles in both the 1.26 and $1.64 \mu\text{m}$ regions, where we identify [Fe II] 1.257 and $1.644 \mu\text{m}$ as the dominant lines contributing to each region. The shape and tilt of these line profiles are correlated within each SN, while there is a variation of tilt shape and width between different 03fg-like SNe.

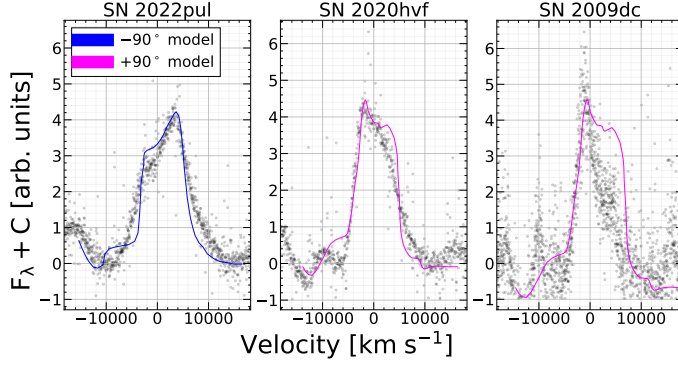


Figure 9. Comparison of off center DDT explosion models from Hoefflich et al. (2021) overlaid with spectral observations of the $1.644 \mu\text{m}$ features of SN 2009dc, SN 2020hvf, and SN 2022pul. Note that the model spectra were adjusted in both flux scale and velocity space for comparison purpose, see the text for more details.

The analysis here suggests that asymmetric chemical distributions may be a common feature in 03fg-like SNe. We provide five quantitative methods for measuring the asymmetry and tilt in the spectra of the 03fg-like SNe. Through these methods, we show that *i*) the peak velocities of both the $1.257 \mu\text{m}$ and $1.644 \mu\text{m}$ features vary between -2000 to $+3000 \text{ km s}^{-1}$ within our sample; *ii*) the tilts m_T of the $1.257 \mu\text{m}$ and $1.644 \mu\text{m}$ features are consistent within 03fg-like SNe but can vary between them; *iii*) the residuals of 03fg-like SNe against normal SNe visually demonstrate a wide variety in the asymmetries of chemical distributions of 03fg-like SNe; *iv*) multi-Gaussian fits demonstrate that, if spectral feature asymmetries are assumed to come from overlapping Gaussian emitting regions, the velocity separation of coupled components is consistent between features for each 03fg-like SN; and *v*) comparison to pre-existing off-center DDT explosion models suggests that 03fg-like SNe produce asymmetric chemical distributions which may be consistent with an off-center DDT scenario.

These methods for measuring line profile asymmetry can be used to analyze future observations, even beyond the nebular-NIR domain. We must stress, though, that the process of multi-Gaussian fitting under the assumption of separate Gaussian emitting regions is not always physical when analyzing asymmetric chemical distributions (see Section 4.5). Additionally, we note that without detailed 3D NLTE modeling and a larger sample size of data, we cannot rule out that other spectral lines are contributing to the profiles in a way which it coincidentally appears that [Fe II] is the dominant ion in both the $1.257 \mu\text{m}$ and $1.644 \mu\text{m}$ regions.

Overall, there are two main models which could produce the line profiles presented in this work: the first

is the merger of two WDs (e.g. Kwok et al. 2024), and the second is an off-center DDT explosion in the core degenerate scenario (e.g. Lu et al. 2021; Hoefflich et al. 2021). While it is outside the scope of this work to produce those models, we can speculate on what differs them. The global (not chemical) asymmetries between the models will differ (i.e. the core degenerate scenario is globally spherical, while the merger of two WDs is not). Only by combining early time continuum polarization measurements with medium-resolution late-time NIR spectra can these models be distinguished. Regardless of this, it is clear that significant advances in our understanding of the physics of the SNe Ia can be made through analysis of NIR line profiles. Observationally speaking, however, the sample size is still small, and it is clear that additional medium-resolution NIR spectra are required to draw more robust conclusions.

C.A, P.H., E.B., J.D., and K.M. acknowledge support by NASA grants JWST-GO-02114, JWST-GO-02122, JWSTGO-03726, JWST-GO-04436, and JWST-GO-04522. C.A, P.H., E.B., J.D., and K.M. and M.S. acknowledge support by NASA grants JWST-GO-03726, JWST-GO-04436, and JWST-GO-04522. M.D.S. is funded by the Independent Research Fund Denmark (IRFD, grant number 10.46540/2032-00022B) J.L. is supported by NSF-2206523 and DOE No. DE-SC0017955. L.G. acknowledges financial support from AGAUR, CSIC, MCIN and AEI 10.13039/501100011033 under projects PID2023-151307NB-I00, PIE 20215AT016, CEX2020-001058-M, and 2021-SGR-01270.

Some of the data presented here were obtained at Keck Observatory, which is a private 501(c)3 non-profit organization operated as a scientific partnership among the California Institute of Technology, the University of California, and the National Aeronautics and Space Administration. The Observatory was made possible by the generous financial support of the W. M. Keck Foundation.

The authors also wish to recognize and acknowledge the very significant cultural role and reverence that the summit of Mauna Kea has always had within the Native Hawaiian community. We are most fortunate to have the opportunity to conduct observations from this mountain.

Facilities: Keck(NIRES), Magellan Baade(FIRE), VLT(XShooter), Las Cumbres Observatory

Software: `scipy` ([Jones et al. 2001](#); [Fadillah et al. 2021](#))

REFERENCES

- Ashall, C., Lu, J., Hsiao, E. Y., et al. 2021, *ApJ*, 922, 205, doi: [10.3847/1538-4357/ac19ac](https://doi.org/10.3847/1538-4357/ac19ac)
- Ashall, C., Hoefflich, P., Baron, E., et al. 2024, *ApJ*, 975, 203, doi: [10.3847/1538-4357/ad6608](https://doi.org/10.3847/1538-4357/ad6608)
- Blondin, S., Dessart, L., Hillier, D. J., Ramsbottom, C. A., & Storey, P. J. 2023, *Astronomy & Astrophysics*, 678, A170
- Bose, S., Stritzinger, M. D., Ashall, C., et al. 2025, arXiv e-prints, arXiv:2501.04086, doi: [10.48550/arXiv.2501.04086](https://doi.org/10.48550/arXiv.2501.04086)
- Childress, M., Aldering, G., Aragon, C., et al. 2011, *The Astrophysical Journal*, 733, 3
- Cushing, M. C., Vacca, W. D., & Rayner, J. T. 2004, *PASP*, 116, 362, doi: [10.1086/382907](https://doi.org/10.1086/382907)
- DerKacy, J., Ashall, C., Hoefflich, P., et al. 2023, *The Astrophysical Journal Letters*, 945, L2
- Diamond, T., Hoefflich, P., Hsiao, E., et al. 2018, *The Astrophysical Journal*, 861, 119
- Diamond, T. R., Hoefflich, P., & Gerardy, C. L. 2015, *The Astrophysical Journal*, 806, 107
- Dimitriadis, G., Maguire, K., Karambelkar, V. R., et al. 2023, *MNRAS*, 521, 1162, doi: [10.1093/mnras/stad536](https://doi.org/10.1093/mnras/stad536)
- Fadillah, M. H. A. Z., Idrus, B., & Hasan, M. K. 2021
- Filippenko, A. V., Richmond, M. W., Branch, D., et al. 1992a, *Astronomical Journal* (ISSN 0004-6256), vol. 104, no. 4, p. 1543-1556, 1684., 104, 1543
- Filippenko, A. V., Richmond, M. W., Matheson, T., et al. 1992b, *Astrophysical Journal*, Part 2-Letters (ISSN 0004-637X), vol. 384, Jan. 1, 1992, p. L15-L18., 384, L15
- Fink, M., Hillebrandt, W., & Röpke, F. 2007, *Astronomy & Astrophysics*, 476, 1133
- Ganeshalingam, M., Li, W., Filippenko, A. V., et al. 2012, *The Astrophysical Journal*, 751, 142
- Hachinger, S., Mazzali, P. A., Taubenberger, S., et al. 2012, *Monthly Notices of the Royal Astronomical Society*, 427, 2057
- Hillebrandt, W., & Niemeyer, J. C. 2000, *ARA&A*, 38, 191, doi: [10.1146/annurev.astro.38.1.191](https://doi.org/10.1146/annurev.astro.38.1.191)
- Hoefflich, P., Hsiao, E. Y., Ashall, C., et al. 2017, *ApJ*, 846, 58, doi: [10.3847/1538-4357/aa84b2](https://doi.org/10.3847/1538-4357/aa84b2)
- Hoefflich, P., Ashall, C., Fisher, A., et al. 2019, in *Nuclei in the Cosmos XV*, Springer, 187–194
- Hoefflich, P., Ashall, C., Bose, S., et al. 2021, *The Astrophysical Journal*, 922, 186
- Holcomb, C., Guillochon, J., De Colle, F., & Ramirez-Ruiz, E. 2013, *The Astrophysical Journal*, 771, 14
- Hoogendam, W., Shappee, B., Brown, P., et al. 2024, *The Astrophysical Journal*, 966, 139
- Howell, A. D., Sullivan, M., Nugent, P. E., et al. 2006, *Nature*, 443, 308
- Howell, D. A. 2001, *The Astrophysical Journal*, 554, L193
- Hoyle, F., & Fowler, W. A. 1960, *ApJ*, 132, 565, doi: [10.1086/146963](https://doi.org/10.1086/146963)
- Hsiao, E., Hoefflich, P., Ashall, C., et al. 2020, *The Astrophysical Journal*, 900, 140
- Iben Jr, I., & Tutukov, A. V. 1984, *Astrophysical Journal*, Part 1 (ISSN 0004-637X), vol. 284, Sept. 15, 1984, p. 719-744., 284, 719
- Jerkstrand, A. 2017, in *Handbook of Supernovae*, ed. A. W. Alsabti & P. Murdin, 795, doi: [10.1007/978-3-319-21846-5_29](https://doi.org/10.1007/978-3-319-21846-5_29)
- Jiang, J.-a., Maeda, K., Kawabata, M., et al. 2021, *ApJL*, 923, L8, doi: [10.3847/2041-8213/ac375f](https://doi.org/10.3847/2041-8213/ac375f)
- Jones, E., Oliphant, T., et al. 2001
- Kashi, A., & Soker, N. 2011, *Monthly Notices of the Royal Astronomical Society*, 417, 1466
- Khan, R., Stanek, K., Stoll, R., & Prieto, J. 2011, *The Astrophysical Journal Letters*, 737, L24
- Kumar, S. 2024, in *American Astronomical Society Meeting Abstracts*, Vol. 243, American Astronomical Society Meeting Abstracts, 232.03
- Kumar, S., Hsiao, E. Y., Ashall, C., et al. 2023, *The Astrophysical Journal*, 945, 27
- Kwok, L. A., Siebert, M. R., Johansson, J., et al. 2024, *The Astrophysical Journal*, 966, 135
- Li, W., Filippenko, A. V., Treffers, R. R., et al. 2001, *The Astrophysical Journal*, 546, 734
- Li, W., Filippenko, A. V., Chornock, R., et al. 2003, *Publications of the Astronomical Society of the Pacific*, 115, 453
- Liu, D., Wang, B., Wu, C., & Han, Z. 2017, *Astronomy & Astrophysics*, 606, A136
- Liu, J., Wang, X., Yang, Y., et al. 2025, arXiv preprint arXiv:2502.18900
- Liu, Z.-W., Röpke, F. K., & Han, Z. 2023, *Research in Astronomy and Astrophysics*, 23, 082001
- Livio, M., & Mazzali, P. 2018, *PhR*, 736, 1, doi: [10.1016/j.physrep.2018.02.002](https://doi.org/10.1016/j.physrep.2018.02.002)
- Livio, M., & Riess, A. G. 2003, *The Astrophysical Journal*, 594, L93
- Lu, J., Ashall, C., Hsiao, E. Y., et al. 2021, *ApJ*, 920, 107, doi: [10.3847/1538-4357/ac1606](https://doi.org/10.3847/1538-4357/ac1606)
- Maeda, K., Jiang, J.-a., Doi, M., Kawabata, M., & Shigeyama, T. 2023, *Monthly Notices of the Royal Astronomical Society*, 521, 1897
- Maeda, K., Benetti, S., Stritzinger, M., et al. 2010, *Nature*, 466, 82

- Maguire, K., Sim, S., Shingles, L., et al. 2018, *Monthly Notices of the Royal Astronomical Society*, 477, 3567
- Marietta, E., Burrows, A., & Fryxell, B. 2000, *The Astrophysical Journal Supplement Series*, 128, 615
- Mazzali, P., Danziger, I., & Turatto, M. 1995, *Astronomy and Astrophysics*, v. 297, p. 509, 297, 509
- Mazzali, P. A., Ropke, F. K., Benetti, S., & Hillebrandt, W. 2007, *Science*, 315, 825
- Noebauer, U., Taubenberger, S., Blinnikov, S., Sorokina, E., & Hillebrandt, W. 2016, *Monthly Notices of the Royal Astronomical Society*, 463, 2972
- Pakmor, R., Hachinger, S., Röpke, F., & Hillebrandt, W. 2011, *Astronomy & Astrophysics*, 528, A117
- Pakmor, R., Kromer, M., Röpke, F. K., et al. 2010, *Nature*, 463, 61
- Pakmor, R., Kromer, M., Taubenberger, S., et al. 2012, *The Astrophysical Journal Letters*, 747, L10, doi: [10.1088/2041-8205/747/1/L10](https://doi.org/10.1088/2041-8205/747/1/L10)
- Penney, R., & Hoefflich, P. 2014, *The Astrophysical Journal*, 795, 84
- Penney, R., & Hoefflich, P. 2014, *ApJ*, 795, 84, doi: [10.1088/0004-637X/795/1/84](https://doi.org/10.1088/0004-637X/795/1/84)
- Siebert, M. R., Dimitriadis, G., Polin, A., & Foley, R. J. 2020, *The Astrophysical Journal Letters*, 900, L27
- Siebert, M. R., Kwok, L. A., Johansson, J., et al. 2023, *The Astrophysical Journal*, 960, 88
- Siebert, M. R., Foley, R. J., Zenati, Y., et al. 2023, *ApJ*, 958, 173, doi: [10.3847/1538-4357/ad037f](https://doi.org/10.3847/1538-4357/ad037f)
- Silverman, J. M., Ganeshalingam, M., Li, W., et al. 2011, *Monthly Notices of the Royal Astronomical Society*, 410, 585
- Soker, N. 2019, *New Astronomy Reviews*, 87, 101535
- Srivastav, S., Smartt, S. J., Huber, M. E., et al. 2023, *ApJL*, 943, L20, doi: [10.3847/2041-8213/acb2ce](https://doi.org/10.3847/2041-8213/acb2ce)
- Taubenberger, S., Benetti, S., Childress, M., et al. 2011, *Monthly Notices of the Royal Astronomical Society*, 412, 2735
- Taubenberger, S., Kromer, M., Hachinger, S., et al. 2013, *Monthly Notices of the Royal Astronomical Society*, 432, 3117
- Taubenberger, S., Floers, A., Vogl, C., et al. 2019, *Monthly Notices of the Royal Astronomical Society*, 488, 5473
- Tucker, M. A., Shappee, B. J., Vallely, P. J., et al. 2020, *MNRAS*, 493, 1044, doi: [10.1093/mnras/stz3390](https://doi.org/10.1093/mnras/stz3390)
- Wang, B., & Han, Z. 2012, *New Astronomy Reviews*, 56, 122
- Webbink, R. 1984, *Astrophysical Journal*, Part 1 (ISSN 0004-637X), vol. 277, Feb. 1, 1984, p. 355-360., 277, 355